



# Multi-physical quantity sensing based on magnetized plasma spherical photonic crystals with evanescent wave

Jie Xu<sup>1</sup> , Tian-Qi Zhu<sup>1</sup> and Hai-Feng Zhang\* 

College of Electronic and Optical Engineering & College of Flexible Electronics (Future Technology), Nanjing University of Posts and Telecommunications, Jiangsu province 210023, People's Republic of China

E-mail: [hanlor@163.com](mailto:hanlor@163.com) and [hanlor@njupt.edu.cn](mailto:hanlor@njupt.edu.cn)

Received 7 August 2023, revised 11 September 2023

Accepted for publication 21 September 2023

Published 28 September 2023



CrossMark

## Abstract

In this paper, a novel structure of magnetized plasma spherical photonic crystals is proposed that enables the development of sensors based on the evanescent wave principle. This sensor structure integrates plasma with two isotropic media and applies periodic boundary conditions. Leveraging the principle of the evanescent wave, when the incident light is perpendicular to the interface of a medium with high optical density or thickness and the incident angle exceeds a critical angle, the transfer matrix method is utilized to compute the sharp peaks in the transmission spectrum. Subsequently, sensors produced using these sharp absorption peaks can detect the magnetic induction intensity, plasma frequency, and solution concentration of serum creatinine. The sensitivity and quality factors of these measurements are  $8.35 \times 10^{10} \text{ T}^{-1}$ , 3583,  $1.5 \times 10^{-4} (2\pi c/d)^{-1}$ , 2970, 3.55, and 22 824, respectively. Furthermore, a detection limit of  $9.155 02 \times 10^{-6} \text{ RIU}$  should be taken into account to ensure the normal operation of serum creatinine detection, satisfying the minimum requirements of biosensing.

Keywords: spherical photonic crystals, evanescent wave, magnetized plasma, serum creatinine sensing

(Some figures may appear in colour only in the online journal)

## 1. Introduction

In physics, Yablonovitch, and John were first involved in the study of photonic crystals (PCs) between the propagation behavior of light and the periodical dielectric structure of materials at the end of the 18th [1, 2]. PCs are periodic structures that manipulate the propagation of light, while spherical photonic crystals (SPCs) specifically refer to PCs with a spherical geometry. SPCs inherit the properties of PCs but also possess additional characteristics related to their spherical symmetry. SPC is a material with a periodic structure that exhibits optical properties in three-dimensional space. Unlike

conventional optical materials, SPCs have a periodic structure that is on the order of the wavelength of incident light. This structure is achieved by arranging a series of spherical particles with specific refractive indices at regular intervals [3]. The optical properties of SPCs arise from the fundamental principles of Bragg diffraction observed in crystalline structures [4]. When an incident light beam traverses the SPCs, it experiences diffraction phenomena attributable to the inherent periodicity of the structure. Consequently, the light beam exhibits complete reflection or selective propagation within distinct incident angles and frequency ranges [5]. The frequency and directionality selectivity inherent in the light propagation characteristics establish SPCs as highly desirable materials for kinds of practical applications, including optical filters, optical waveguides, and optical mirrors [6–8]. The most

<sup>1</sup> Jie Xu and Tian-Qi Zhu contribute equally to this article.

\* Author to whom any correspondence should be addressed.

prominent characteristic of SPCs is that they have an electron band structure similar to those in semiconductors and metals. In the material, there exist photon bands that allow propagation through the material and photonic band gap that does not [9]. Based on these features, the optical flow can be accurately controlled, and because of the simple structure, flexible design, small size, and other advantages, it is used to make optical device wave absorbers, antennas, and sensors [10–12]. The research on PCs sensors is an active and rapidly developing field [13–15]. Scientists are continuously exploring new materials, structures, and detection techniques to enhance the sensitivity ( $S$ ) and stability of these sensors for various applications. Recent studies have focused on developing PCs sensors for detecting biomolecules, such as proteins, DNA, and viruses, in biological fluids for medical diagnostics [16–18].

Evanescent waves are electromagnetic waves (EWs) that exist near the interface between two media and decay exponentially away from the interface, without propagating into the second medium [19]. They are generated when a light beam is incident at an angle on a surface that has a higher refractive index (RI) than the surrounding medium, and the wave penetrates the surface but is reflected into the first medium. In sensing, evanescent waves have been utilized to detect changes in the RI of a material, which can be used to monitor chemical reactions or biological processes [20]. The conditions for the generation of evanescent waves are limited. Usually, we can obtain the propagation of evanescent waves by adding a prism to the design structure. By incorporating a prism into the setup, it becomes possible to illuminate the interface at an angle exceeding the critical angle, facilitating total internal reflection within the prism. As a result, the evanescent waves can propagate along the prism's interface with the surrounding medium. The angle and position of the prism can be finely adjusted to precisely control the characteristics and direction of the evanescent waves [21]. This technique finds extensive utility across various domains, including evanescent wave spectroscopy, near-field microscopy, and surface plasmon resonance sensing [22–24]. Researchers leverage this method to explore and manipulate the properties of evanescent waves, which carry valuable insights into the near-field interactions and surface properties of materials.

Magnetized plasma is a unique state of matter that has garnered significant attention in the photonics community due to its exceptional electrical, optical, and magnetic properties [25]. It is plasma that has been subjected to an external magnetic field, resulting in the confinement of charged particles along the field lines. This confinement can attribute to a variety of interesting and complex phenomena, for example, the formation of magnetic flux tubes, the development of plasma waves, and the generation of strong electromagnetic radiation. Researchers in the field of photonics have been particularly interested in the use of magnetized plasma for various applications, including plasma-based particle accelerators and magnetic fusion energy research [26, 27]. The solution concentration of serum creatinine ( $C_{SC}$ ) is an important marker of kidney function, as it reflects the ability of the kidneys to filter waste products out of the blood. Measuring  $C_{SC}$  is a common part of routine blood testing, and it is used to help diagnose

and monitor a variety of kidney-related conditions, such as chronic kidney disease, acute kidney injury, and kidney failure. It is also used to adjust medication dosages for drugs that are cleared by the kidneys [28].

Previous studies have demonstrated the widespread utilization of PCs in sensor production. While traditional two-dimensional PCs sensors have shown remarkable performance in areas such as non-reciprocity and biochemical sensing, they still exhibit certain limitations and drawbacks [29, 30]. Furthermore, these challenges are constrained by the limitations of structural design and cannot be fully addressed by the integration of various physical principles alone. The most effective approach is to extend the design structure into a three-dimensional coordinate system, thereby expanding upon the concepts of cylindrical PCs and SPCs [31, 32]. SPCs exhibit several advantages over conventional two-dimensional PCs in sensor applications. Their unique three-dimensional structure enhances the interaction between light and matter, resulting in a longer interaction path length and increased sensitivity. Additionally, they possess a larger sensing volume, enabling the detection of a greater number of analytes and improving the overall detection capabilities. The versatile design options offered by SPCs allow for precise control over spectral response and directionality, while also minimizing surface-related effects, leading to improved reliability. These inherent advantages position SPCs as a promising platform for high-performance sensors, offering enhanced sensitivity and the ability to manipulate light with precision.

In this paper, a multi-physical quantity sensor based on the evanescent wave is proposed. When the light passes through the prism to form an evanescent wave, it is inserted into the design structure to form a sharp transmission peak for the design of a multi-physical quantity sensor. According to the principle of frequency modulation, after changing the sensing variable, the transmission peak will generate the corresponding displacement in the working frequency band, which can meet the basic requirements of making sensors. Because the magnetized plasma material is involved in the structure, it can be used to detect the plasma frequency ( $PF$ ) and magnetic field induction intensity ( $B$ ). Due to the  $S$  of the structure to RI, it can also be used to make biological detection of  $C_{SC}$ . The superimposed multiple theories allow this sensor to have a good  $S$  value, a higher quality factor ( $Q$ ), and a figure of merit ( $FOM$ ).

## 2. Design of MPSPC

### 2.1. Configuration of MPSPC

The proposed magnetized plasma spherical photonic crystals (MPSPCs) which are a multifunctional new sensing structure consisting of six layered structures and two prisms that can measure among  $B$ ,  $PF$ , and  $C_{SC}$  is plotted in figure 1(a). The MPSPC is mainly composed of a unit structure consisting of three media with two periodic structures. This periodic arrangement is widely used in PCs sensing design due to the advantages of phase adjustment. The unit structure consists of two isotropic media A and B with RI of 2.8 (Titanium

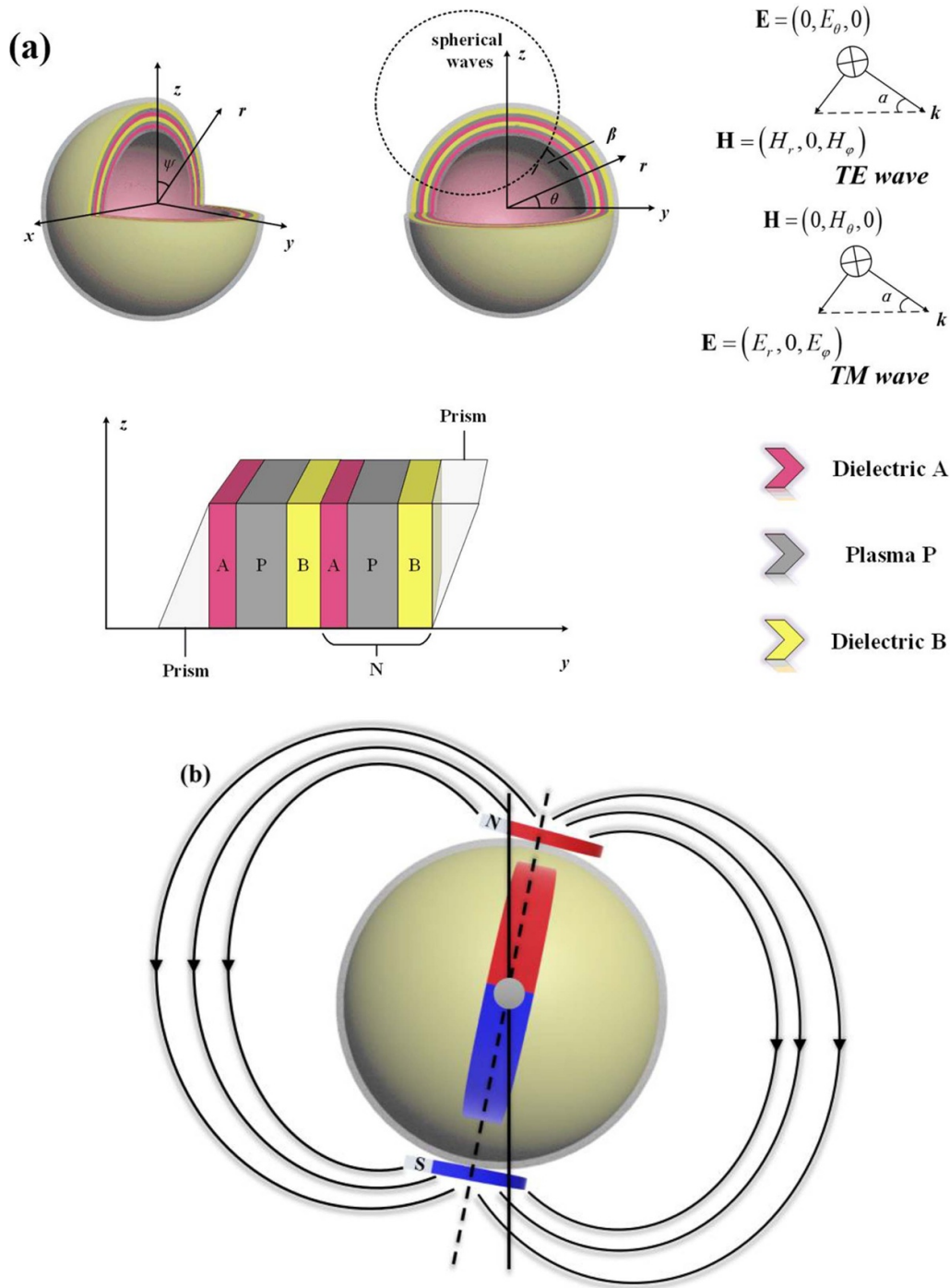


**Figure 1.** (a) The structure atlas of designed MPSPC. (b) The way magnetic fields are applied.

Dioxide) and 2.1 (Zirconium Dioxide) respectively, and a layer of P which stands for plasma is placed in the sandwich between the two. To illustrate the practicality of plasma, it is essential to delve into their fabrication process. It is widely acknowledged, particularly in the context of closed-cycle magnetohydrodynamic generation, that seed materials like cesium and potassium, when subjected to non-equilibrium conditions, yield highly efficient generator performance. Therefore, in the preparatory stages, it is advisable to initiate the process with alkali metals or compositions containing alkali metals as seed

materials. Subsequently, helium is introduced as the working gas. This sequential approach is preferred due to its ability to mitigate seed ionization instability and partial ionization issues in inert gases, thus ensuring the achievement of a stable and uniform plasma state [33]. The media A and B are primarily selected due to their favorable optical properties, including excellent dispersion characteristics and high RIs. Additionally, both materials possess high melting points, exhibit resistance to high temperatures, and demonstrate good chemical stability [34, 35]. These attributes collectively reduce the constraints on

potential application scenarios, making them suited choices for our research. As for the numerical setting of the effective permeability of  $PF$ , it is very special for SPCs, and specific details will be described in detail later. In the setting of thickness, we adopt the idea of normalization to simplify the data. Medium A, P, and B are 0.24d, 0.32d, and 0.44d, respectively. For a more scientifically rigorous design of the structure, it is imperative to elucidate the application of the magnetic field within the proposed configuration. As depicted in figure 1(b), two electromagnets are positioned at a tilt of 11.5 degrees each, akin to the orientation of the Earth's north and south magnetic poles. This arrangement serves to establish an optimal magnetic field condition both inside and outside the spherical structure, aligning precisely with the prerequisites of this design.

### 2.2. Transfer matrix method (TMM) of MPSPCs

The computation of absorption, reflection, and transmission of MPSPCs combined with plasma is influenced by the unique geometric properties of the sphere, as well as the considerations of trace elements and the definition of the incident angle [36]. In this investigation, the TM waves are precisely defined by utilizing the profile of the spherical wave and the proposed MPSPCs aligned with the direction of wave propagation. In this particular plane, the electric field  $E$  is perpendicular to the plane, while the magnetic field  $H$  runs parallel to it, with the wave vector  $G$  indicating the propagation direction. It is worth highlighting the presence of an intersecting point between the MPSPCs and the spherical waves. In figure 1(a), tangents are drawn from this point of intersection to both the MPSPCs and the spherical waves, allowing for the determination of the angle of incidence. The EWs propagate from the plane which perpendicular to the  $X$ -axis at an incidence angle  $\alpha$ . Notably, in TM polarization, the electric field  $\mathbf{E}$  consistently maintains its perpendicular orientation to the wave vector  $G$ .

The differential form of Maxwell's system of equations can be mathematically expressed as [37]:

$$\nabla \times \mathbf{E} = -\mu_0 \frac{\partial \mathbf{H}}{\partial t} \quad (1)$$

$$\nabla \times \mathbf{H} = \varepsilon_0 \frac{\partial \mathbf{E}}{\partial t} + \mathbf{J} \quad (2)$$

$$\frac{d\mathbf{J}}{dt} + \nu_c \mathbf{J} = \varepsilon_0 \omega_p^2 \mathbf{E} + \omega_c \times \mathbf{J} \quad (3)$$

where  $J$  is referred to as the polarization current density and is a vector that decomposes along the  $l$ ,  $\alpha$ , and  $\psi$  directions. The frequency of collision is denoted by  $\nu_c$  and the plasma frequency is denoted by  $\omega_p$ .  $\omega_c$  is the plasma cyclotron frequency, noted as  $eB_0/m_e\alpha$ . Initially, normalized frequency is used in this paper to simplify the calculation,  $\omega_0 = 2\pi c/d$ ,  $\omega_p = \omega_0$ ,  $\nu_c = 0.0001\omega_p$ , and  $\omega_c = 0$ .

Utilizing the vector relationship, decomposing equation (3) in the three different coordinate components of  $l$ ,  $\alpha$ , and  $\psi$ , we can obtain:

$$(-i\omega + \nu_c)J_l = \varepsilon_0 \omega_p^2 E_l + \omega_c J_\varphi \quad (4)$$

$$(-i\omega + \nu_c)J_\theta = \varepsilon_0 \omega_p^2 E_\theta \quad (5)$$

$$(-i\omega + \nu_c)J_\varphi = \varepsilon_0 \omega_p^2 E_\varphi - \omega_c J_l. \quad (6)$$

Combining the knowledge about determinants, the relationship between  $J$  and  $E$  is formulated as [38]:

$$\begin{pmatrix} J_r \\ J_\theta \\ J_\varphi \end{pmatrix} = \varepsilon_0 \begin{pmatrix} \frac{i\omega_p^2(\omega+iv_c)}{(\omega+iv_c)^2-\omega_c^2} & 0 & -\frac{\omega_p^2\omega_c}{(\omega+iv_c)^2-\omega_c^2} \\ 0 & \frac{i\omega_p^2}{\omega+iv_c} & 0 \\ \frac{\omega_p^2\omega_c}{(\omega+iv_c)^2-\omega_c^2} & 0 & \frac{i\omega_p^2(\omega+iv_c)}{(\omega+iv_c)^2-\omega_c^2} \end{pmatrix} \begin{pmatrix} E_l \\ E_\alpha \\ E_\varphi \end{pmatrix}. \quad (7)$$

From the above, it can be obtained that

$$\nabla \times \mathbf{H} = \varepsilon_0 \varepsilon_p \frac{\partial \mathbf{E}}{\partial t} \quad (8)$$

where,

$$\varepsilon_p = \begin{pmatrix} \varepsilon_1 & 0 & i\varepsilon_2 \\ 0 & \varepsilon_3 & 0 \\ -i\varepsilon_2 & 0 & \varepsilon_1 \end{pmatrix} \quad (9)$$

$$\varepsilon_1 = 1 - \frac{\omega_p^2(\omega+iv_c)}{\omega[(\omega+iv_c)^2-\omega_c^2]} \quad (10)$$

$$\varepsilon_2 = -\frac{\omega_p^2\omega_c}{\omega[(\omega+iv_c)^2-\omega_c^2]} \quad (11)$$

$$\varepsilon_3 = 1 - \frac{\omega_p^2}{\omega(\omega+iv_c)}. \quad (12)$$

Under the TM polarization, the  $E$  and  $H$  are represented as:

$$\mathbf{E} = e^{-i\omega t} (E_l, 0, E_\varphi) \quad (13)$$

$$\mathbf{H} = e^{-i\omega t} (0, H_\alpha, 0). \quad (14)$$

The relative calculation is carried out by combining Maxwell's equations:

$$\frac{1}{l \sin \alpha} \left[ \frac{\partial E_l}{\partial \varphi} - \frac{\partial}{\partial l} (l \sin \alpha E_\varphi) \right] = -i\omega \mu_0 H_\alpha \quad (15)$$

$$\frac{1}{l^2 \sin \alpha} \left[ \frac{\partial}{\partial \alpha} (l \sin \alpha H_\varphi) - \frac{\partial}{\partial \varphi} (l H_\alpha) \right] = i\omega \varepsilon_0 (\varepsilon_1 E_l + i\varepsilon_2 E_\varphi) \quad (16)$$

$$\frac{1}{l} \left[ \frac{\partial}{\partial l} (l H_\alpha) - \frac{\partial H_l}{\partial \alpha} \right] = i\omega \varepsilon_0 (-i\varepsilon_2 E_l + \varepsilon_1 E_\varphi). \quad (17)$$

Due to the physical characteristics of spherical waves, the derivative of  $\psi$  should be correction treatment. Here, the above equation becomes:

$$\frac{1}{\rho^2 \sin \alpha} \left[ -\frac{\partial}{\partial \varphi} (lH_\alpha) \right] = i\omega \varepsilon_0 (\varepsilon_1 E_l + i\varepsilon_2 E_\varphi) \quad (18)$$

$$\frac{1}{l} \left[ \frac{\partial}{\partial l} (rH_\theta) \right] = i\omega \varepsilon_0 (-i\varepsilon_2 E_r + \varepsilon_1 E_\varphi). \quad (19)$$

Substitute equations (18) and (19) into equation (15)

$$\frac{1}{\rho^2} \frac{\partial}{\partial l} \left( \rho^2 \frac{\partial H_\alpha}{\partial l} \right) + \frac{1}{\rho^2 \sin^2 \alpha} \frac{\partial^2 H_\alpha}{\partial \varphi^2} + G^2 H_\alpha = 0. \quad (20)$$

Furthermore, here

$$G = \omega \cos \alpha \sqrt{\mu_0 \varepsilon_0 \varepsilon_{TM}} \quad (21)$$

$$\varepsilon_{TM} = (\varepsilon_1^2 - \varepsilon_2^2) / \varepsilon_1 \quad (22)$$

and  $\alpha$  is the incident angle. Then we define

$$H_\alpha(x) = V(x) \Psi(\varphi) \quad (23)$$

where  $x = Gl$ . It is readily known that  $H_\alpha$  fulfills the following differential equation

$$\frac{d^2 \Psi}{d\varphi^2} + f^2 \Psi = 0. \quad (24)$$

Solving differential equation (24) yields,

$$\Psi \sim e^{if\varphi} \quad (25)$$

where  $f$  is a positive integer, a negative integer, and zero.

Then let,

$$f^2 = l(l+1) \sin^2 \alpha. \quad (26)$$

Utilizing the separation of variables method, the equations on  $V(x)$  are derived by combining equations (23), (24) and (26)

$$x^2 \frac{d^2 V}{dx^2} + x \frac{dV}{dx} + \left[ x^2 - \left( l + \frac{1}{2} \right)^2 \right] V(x) = 0. \quad (27)$$

The boundary conditions are employed to derive the analytic equation of  $V(x)$ , which consists of standard semi-odd order spherical Bessel equations

$$V(x) = A j_{le}(x) + B n_{le}(x). \quad (28)$$

The solutions to the spherical Bessel equation of semi-odd order are obtained, and the corresponding expressions are provided below:

$$\begin{aligned} j_{le}(x) &= \sqrt{\frac{\pi}{2x}} J_{le+\frac{1}{2}}(x) \\ n_{le}(x) &= \sqrt{\frac{\pi}{2x}} N_{le+\frac{1}{2}}(x). \end{aligned} \quad (29)$$

Meanwhile,  $j'_{le}(x)$  and  $n'_{le}(x)$  are the first-order derivatives of the Bessel functions, and the corresponding equations are indicated as:

$$\begin{aligned} j'_{le}(x) &= \sqrt{\frac{\pi}{2x}} J'_{le+\frac{1}{2}}(x) - \frac{1}{2} \sqrt{\frac{\pi}{2}} x^{-\frac{3}{2}} J_{le+\frac{1}{2}}(x) \\ n'_{le}(x) &= \sqrt{\frac{\pi}{2x}} N'_{le+\frac{1}{2}}(x) - \frac{1}{2} \sqrt{\frac{\pi}{2}} x^{-\frac{3}{2}} N_{le+\frac{1}{2}}(x). \end{aligned} \quad (30)$$

The vector

$$\begin{pmatrix} V(x) \\ U(x) \end{pmatrix} \quad (31)$$

is stipulated and the TMM is adopted to relate the homologous vectors at different radius [39]

$$\begin{pmatrix} V(x) \\ U(x) \end{pmatrix} = \mathbf{M} \begin{pmatrix} V(x_0) \\ U(x_0) \end{pmatrix} = \begin{pmatrix} M_{11} & M_{12} \\ M_{21} & M_{22} \end{pmatrix} \begin{pmatrix} V(x_0) \\ U(x_0) \end{pmatrix}. \quad (32)$$

To make the calculation easier, the method of taking special values is employed. In the first place, let,

$$V(x_0) = 1, U(x_0) = 0. \quad (33)$$

Assign values to  $V(x)$  and  $U(x)$

$$\begin{aligned} V(x_0) &= A j_{le}(x_0) + B n_{le}(x_0) = 1 \\ U(x_0) &= A j'_{le}(x_0) + B n'_{le}(x_0) + x_0 A j_{le}'(x_0) + x_0 B n_{le}'(x_0) = 0. \end{aligned} \quad (34)$$

The expressions for A and B can be derived by associating equation (31)

$$\begin{aligned} A &= \frac{1}{j_{le}(x_0) n'_{le}(x_0) - n_{le}(x_0) j'_{le}(x_0)} \left[ n_{le}'(x_0) + \frac{n_{le}(x_0)}{x_0} \right] \\ B &= \frac{1}{n_{le}(x_0) j'_{le}(x_0) - n'_{le}(x_0) j_{le}(x_0)} \left[ j_{le}'(x_0) + \frac{j_{le}(x_0)}{x_0} \right]. \end{aligned} \quad (35)$$

Combining equations (33)–(35), the expressions for  $M_{11}$  and  $M_{21}$  are derived

$$\begin{aligned} M_{11} &= \frac{j_{le}(x)}{j_{le}(x_0) n'_{le}(x_0) - n_{le}(x_0) j'_{le}(x_0)} \left[ n_{le}'(x_0) + \frac{n_{le}(x_0)}{x_0} \right] \\ &+ \frac{n_{le}(x)}{n_{le}(x_0) j'_{le}(x_0) - n'_{le}(x_0) j_{le}(x_0)} \left[ j_{le}'(x_0) + \frac{j_{le}(x_0)}{x_0} \right] \end{aligned} \quad (36)$$

$$\begin{aligned} M_{21} &= \frac{1}{i\omega \varepsilon r} \left\{ \frac{j_{le}(x)}{j_{le}(x_0) n'_{le}(x_0) - n_{le}(x_0) j'_{le}(x_0)} \left[ n_{le}'(x_0) + \frac{n_{le}(x_0)}{x_0} \right] \right. \\ &+ \frac{n_{le}(x)}{n_{le}(x_0) j'_{le}(x_0) - n'_{le}(x_0) j_{le}(x_0)} \left[ j_{le}'(x_0) + \frac{j_{le}(x_0)}{x_0} \right] \\ &+ \frac{x j_{le}'(x)}{j_{le}(x_0) n'_{le}(x_0) - n_{le}(x_0) j'_{le}(x_0)} \left[ n_{le}'(x_0) + \frac{n_{le}(x_0)}{x_0} \right] \\ &\left. + \frac{x n_{le}'(x)}{n_{le}(x_0) j'_{le}(x_0) - n'_{le}(x_0) j_{le}(x_0)} \left[ j_{le}'(x_0) + \frac{j_{le}(x_0)}{x_0} \right] \right\}. \end{aligned} \quad (37)$$

Similarly, assigning values to  $V(x)$  and  $U(x)$ ,

$$V(x_0) = 0, U(x_0) = 1. \tag{38}$$

Then we get:

$$\begin{aligned} V(x_0) &= Cj_{le}(x_0) + Dn_{le}(x_0) = 0 \\ U(x_0) &= \frac{1}{i\omega\epsilon l_0} [Cj_{le}(x_0) + Dn_{le}(x_0) + x_0 Cj_{le}'(x_0) \\ &\quad + x_0 Dn_{le}'(x_0)] = 1. \end{aligned} \tag{39}$$

The expressions for coefficients C and D are presented below:

$$\begin{aligned} C &= \frac{1}{n_{le}(x_0)j_{le}'(x_0) - n_{le}'(x_0)j_{le}(x_0)} \left[ \frac{i\omega\epsilon}{G} n_{le}(x_0) \right] \\ D &= \frac{1}{j_{le}(x_0)n_{le}'(x_0) - n_{le}(x_0)j_{le}'(x_0)} \left[ \frac{i\omega\epsilon}{G} j_{le}(x_0) \right]. \end{aligned} \tag{40}$$

Easy to access the expressions for  $M_{12}$  and  $M_{22}$

$$\begin{aligned} M_{12} &= \frac{j_{le}(x)}{n_{le}(x_0)j_{le}'(x_0) - n_{le}'(x_0)j_{le}(x_0)} \left[ \frac{i\omega\epsilon}{G} n_{le}(x_0) \right] \\ &\quad + \frac{n_{le}(x)}{j_{le}(x_0)n_{le}'(x_0) - n_{le}(x_0)j_{le}'(x_0)} \left[ \frac{i\omega\epsilon}{G} j_{le}(x_0) \right] \end{aligned} \tag{41}$$

$$\begin{aligned} M_{22} &= \frac{1}{i\omega\epsilon l} \left\{ \frac{j_{le}(x)}{n_{le}(x_0)j_{le}'(x_0) - n_{le}'(x_0)j_{le}(x_0)} \left[ \frac{i\omega\epsilon}{G} n_{le}(x_0) \right] \right. \\ &\quad + \frac{n_{le}(x)}{j_{le}(x_0)n_{le}'(x_0) - n_{le}(x_0)j_{le}'(x_0)} \left[ \frac{i\omega\epsilon}{G} j_{le}(x_0) \right] \\ &\quad + \frac{xj_{le}'(x)}{n_{le}(x_0)j_{le}'(x_0) - n_{le}'(x_0)j_{le}(x_0)} \left[ \frac{i\omega\epsilon}{G} n_{le}(x_0) \right] \\ &\quad \left. + \frac{xn_{le}'(x)}{j_{le}(x_0)n_{le}'(x_0) - n_{le}(x_0)j_{le}'(x_0)} \left[ \frac{i\omega\epsilon}{G} j_{le}(x_0) \right] \right\}. \end{aligned} \tag{42}$$

At this stage, the expressions for each element of the transfer matrix are derived. In the study of the propagation of light, it is common to define the incident and the outgoing waves in positive and negative directions, which are represented by two Hankel functions

$$\begin{aligned} h_1^{(1)}(x) &= j_{le}(x) + in_{le}(x) \\ h_1^{(2)}(x) &= j_{le}(x) - in_{le}(x). \end{aligned} \tag{43}$$

The  $H$  and  $E$  can be expressed separately as:

$$\begin{aligned} H_\alpha^+(x) &= Qh_{le}^{(2)}(x) e^{if\varphi} \\ H_\alpha^-(x) &= Ph_{le}^{(1)}(x) e^{if\varphi} \\ E_\varphi^+(x) &= \frac{Q}{i\omega\epsilon l} [h_{le}^{(2)}(x) + xh_{le}^{(2)'}(x)] e^{if\varphi} \\ E_\varphi^-(x) &= \frac{P}{i\omega\epsilon l} [h_{le}^{(1)}(x) + xh_{le}^{(1)'}(x)] e^{if\varphi}. \end{aligned} \tag{44}$$

$$\tag{45}$$

From Maxwell's system of equations, the following relationship between the  $E$  and  $H$  can be realized

$$\begin{aligned} C_{le}^{(2)}(x) &= 1 + x \frac{h_{le}^{(2)'}(x)}{h_{le}^{(2)}(x)} \\ C_{le}^{(1)}(x) &= 1 + x \frac{h_{le}^{(1)'}(x)}{h_{le}^{(1)}(x)}. \end{aligned} \tag{46}$$

Within the proposed MPSPCs, the evanescent spherical waves undergo incidence at  $l_0$  and exit at  $r_f$ . The reflection coefficient  $r_d$  and transmission coefficient  $t_d$  can be accurately described by the elements present in the transmission matrix  $M$

$$\begin{pmatrix} 1 + r_d \\ \frac{C_{le}^{(2)}(x_0)}{i\omega\epsilon_0 r_0} + \frac{C_{le}^{(1)}(x_0)}{i\omega\epsilon_0 r_0} r_d \end{pmatrix} = M^{-1} \begin{pmatrix} t_d \\ \frac{C_{le}^{(2)}(x_f)}{i\omega\epsilon_f r_f} t_d \end{pmatrix} \tag{47}$$

where,

$$\begin{aligned} M &= M_1 M_2 M_1 \dots M_1 M_2 \\ M^{-1} &= \begin{pmatrix} M'_{11} & M'_{12} \\ M'_{21} & M'_{22} \end{pmatrix}. \end{aligned} \tag{48}$$

$r_d$  and  $t_d$  are able to be represented by the elements in the transfer matrix  $M$ . The calculate expression is written as:

$$t_d = \frac{C_{le}^{(1)}(x_0) - C_{le}^{(2)}(x_0)}{i\omega\epsilon_0 r_0 \left[ M_{11} \frac{C_{le}^{(1)}(x_0)}{i\omega\epsilon_0 r_0} - M_{21} + \frac{C_{le}^{(2)}(x_f)}{i\omega\epsilon_f r_f} \cdot \frac{C_{le}^{(1)}(x_0)}{i\omega\epsilon_0 r_0} M_{12} - M_{22} \frac{C_{le}^{(2)}(x_f)}{i\omega\epsilon_f r_f} \right]} \tag{49}$$

$$r_d = M_{11} + M_{12} \frac{C_{le}^{(2)}(x_f)}{i\omega\epsilon_f r_f}. \tag{50}$$

Ultimately get,

$$T = |t_d|^2 \quad R = |r_d|^2 \tag{51}$$

$$A = 1 - T - R. \tag{52}$$

### 2.3. The performance of sensor

In this paragraph, the calculation method of sensor performance evaluation is revealed. The commonly used metrics for performance evaluation include  $S$ ,  $Q$ ,  $FOM$ , and detection limit ( $DL$ ). The calculation formulas for these metrics are provided below [40]:

$$S = \frac{\Delta f}{\Delta n} \tag{53}$$

$$Q = \frac{f_T}{FWHM} \tag{54}$$

$$FOM = \frac{S}{FWHM} \tag{55}$$

$$DL = \frac{f_T}{20 \times S \times Q} \quad (56)$$

where  $\Delta f$  and  $\Delta n$  stand for the amount of variation in frequency and RI,  $f_T$  represents the magnitude of the peak frequency, and  $FWHM$  is on behalf of the half-high frequency width of the absorption peak transmission peak. A well-designed sensor tends to have a significant  $S$ ,  $Q$ ,  $FOM$ , and a low  $DL$ . The values of these parameters provide a clear visual representation of the sensing performance.

### 3. Initial parameter of MPSPCs sensor

To construct MPSPCs depicted in figure 1, the initial parameters  $n_a = 2.8$ ,  $n_b = 2.1$ ,  $d_a = 0.24d$ ,  $d_b = 0.32d$ , and  $d_p = 0.44d$  are required, where  $d$  is the normalized length. For the parameter setting of magnetized plasma, we normalize frequency  $\omega_0 = 2\pi c/d$ ,  $\omega_c = 0.8\omega_p$ , and collision frequency  $\nu_c = 0.00001\omega_p$  to simplify the frequency parameter processing. The transmission spectra under these parameter conditions are obtained using the TMM. Due to the periodic arrangement of MPSPCs, it is important to consider the number of periods of the unit containing magnetized plasma by two ordinary media. Figure 2 displays the transmission spectrum complexity for  $N$  (on behalf of the layers of periodic cell structure) = 2, 3, and 4. A single sharp peak with minimized burrs is sought for better performance as a sensor in the operating frequency range of 16–16.6 ( $2\pi c/d$ ). For  $N = 2$ , a single peak occurs at 16.32 ( $2\pi c/d$ ), and the transmittance can reach 0.9947. When  $N = 3$ , the absorption rate is 0.9238 at 16.31 ( $2\pi c/d$ ), and a peak value exists in the subsequent working band.  $N = 4$  results in more sharp peaks, with multiple sharp peaks stacked together at the highest peak. Figure 2 reveals a notable trend, as the number of periods increases, more instances of frequency and phase modulation align with the criteria for generating resonance peaks, specifically integer multiples of half-wavelength. Consequently, the count of observable peaks rises proportionally. Simultaneously, as the number of propagation cycles increases, energy attenuation becomes more pronounced. This augmentation in resonance frequency leads to enhanced transmission efficiency, ultimately yielding sharper transmission peaks. In accordance with the production principle of the sensor, only  $N = 2$  can satisfy the production demand, and thus improve the structure design.

The optimization of the sensor infrastructure has resulted in improved parameters, specifically setting  $\omega_p = \omega_0$  and  $\omega_c = 0.8\omega_p$ . Dielectrics A and B act as two prisms respectively. To assess the generation of evanescent waves in accordance with the principle of high transmission due to the introduced prism structure, a detailed examination of the magnetic field distribution within the structure is conducted. This analysis provides valuable insights into the influence of transmitted evanescent waves based on fundamental physical principles. The magnetic field intensity distribution in the  $z$ -direction depicts the behavior of the incident TM wave's magnetic field

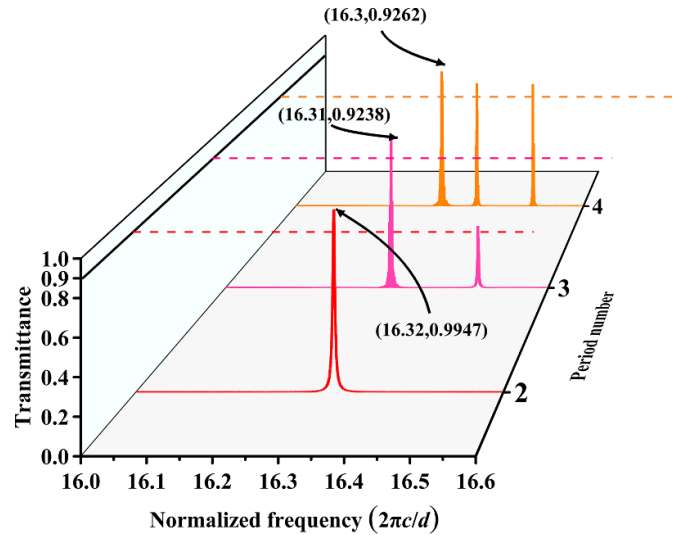


**Figure 2.**  $N = 2, 3$ , and  $4$ , the transmission spectra in the working frequency band are generated by the structure.

intensity at the corresponding frequency of the transmission peak. A notable phenomenon of evanescent wave occurrence arises when EWs penetrate the magnetized plasma layer via the prism. The thinness of this layer allows for full reflection to occur at the boundary between dielectrics A and B. As illustrated in figure 3(a), the electromagnetic field becomes confined within the resonant cavities formed by dielectrics A and B. In the electromagnetic field size distribution simulation of the structure, because the shape of the sphere is not easy to calculate, it is uniformly stretched into cuboid regular arrangement for calculation. This confinement gives rise to a distinct transmission peak in the overall transmission spectrum, signifying the presence of resonant modes. Figure 3(b) displays the dispersion relation of the proposed structure, depicting the Bloch wave vector  $\beta z$  within the range of  $0$  to  $\pi/d$ . Notably, under suitable incident angles, distinct transmission bands can be observed, represented by the black regions in figure 3(b). The dispersion spectrum reveals the presence of two wide white bands, alternating with the black regions. This intriguing arrangement of black and white regions signifies the high and low distribution of transmission spectrum lines. The formation of these transmission bands can be attributed to the existence of evanescent waves, which play a significant role in shaping the passband structures. These unique physical properties give rise to the observed phenomenon, wherein the presence of vanishing waves contributes to the distinctive pattern of the transmission spectrum. The dispersion spectrum, characterized by the distinct alternation of black and white regions, reflects the specific transmission characteristics exhibited by the proposed structure.

### 4. Measurement and discussion

When designing a MPSPCs sensor, it is important to establish a relationship between the frequency and the object being

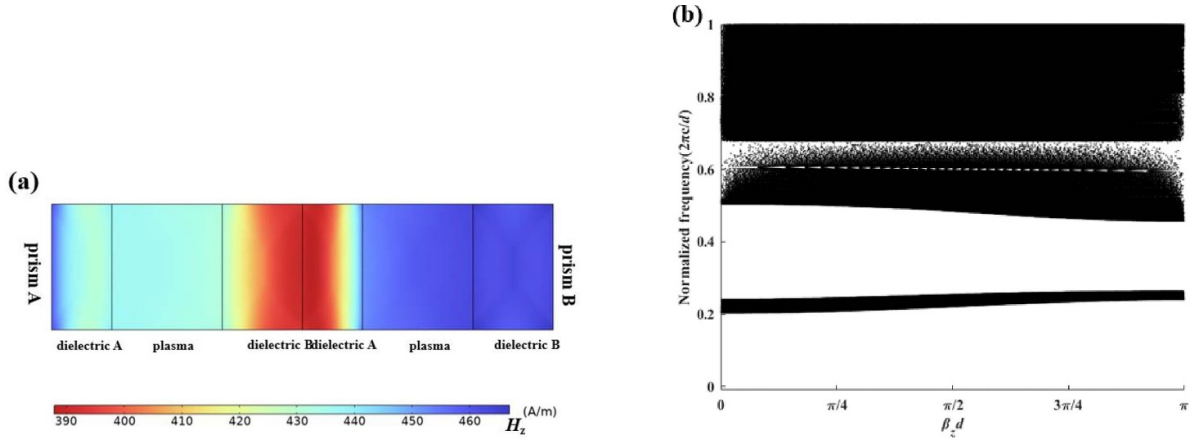


Figure 3. (a) Magnetic field distribution of MPSPCs structure. (b) The transmission frequency ranges with different Bloch wave vectors.

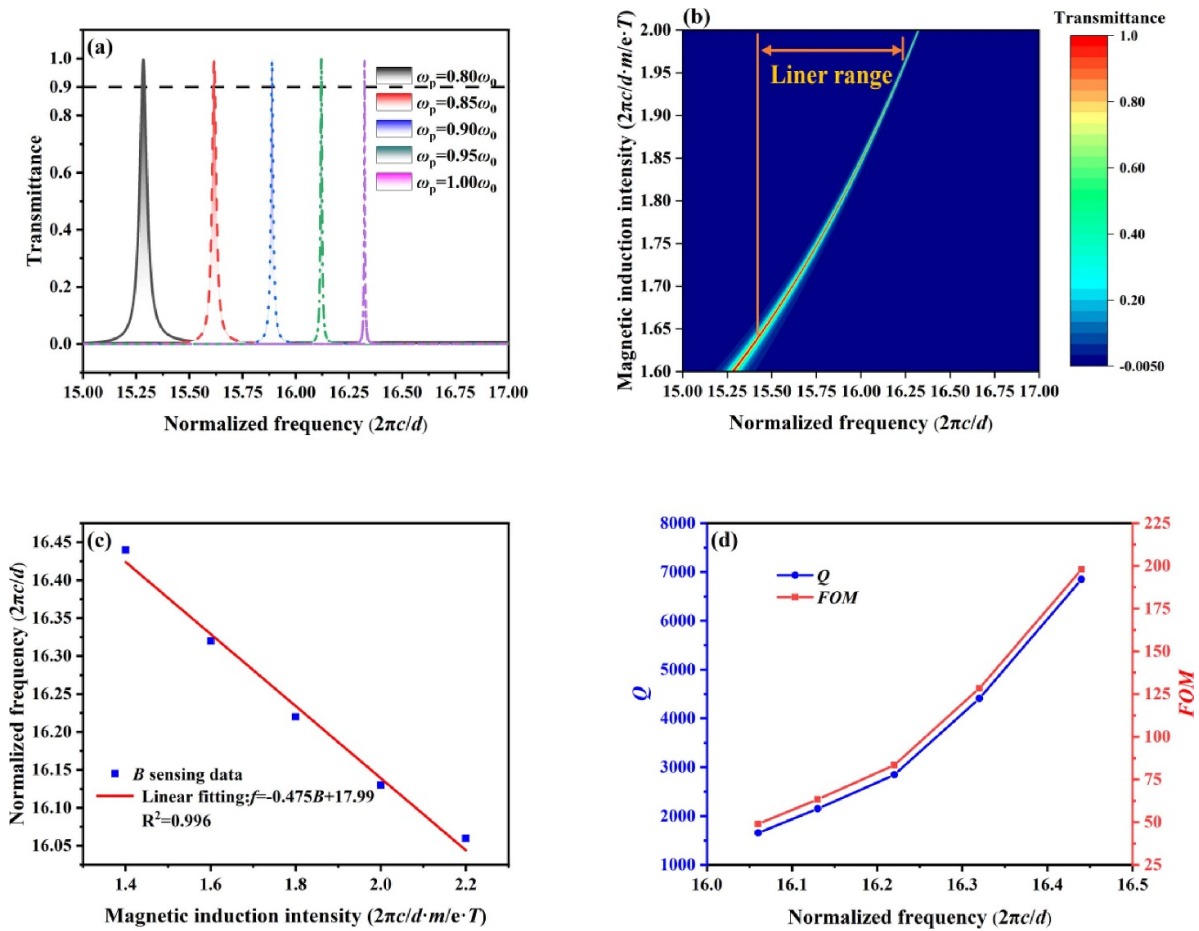


Figure 4. (a) Transmittance peaks of each frequency point under different  $\omega_c$ . (b) Transmittance characteristics of operating frequency range in  $\omega_c$  range. (c) Linear relationship between frequency and range of  $B$  measurement. (d) Variation of  $Q$  and  $FOM$  in  $B$  measuring range.

measured. This allows for the conversion of an unclear signal into a visible photoelectric signal. The resonant frequency must shift linearly with changes in the correlation coefficient of the object being measured. Sensors based on this principle have shown excellent sensing performance. The sensor presented in figure 2 demonstrates high resolution and high-quality sensing performance, allowing for measurements of  $B$ ,  $PF$ , and  $C_{SC}$ . The sensor's performance is on par with that of a biosensor.

#### 4.1. About the magnetic field

To measure the magnetic field  $B$ , we adjust the initial data to  $\omega_c = 1\omega_p$  and varied the size of  $\omega_p$ . The transmission spectra are observed and found that the transmission peak shifted in frequency with different  $\omega_p$  values, as shown in figure 4(a). We vary  $\omega_p$  from  $0.8\omega_0$  to  $1.0\omega_0$  in increments of  $0.05\omega_0$  and performed simulation calculations. The peak frequency of the transmission spectrum shows a certain functional relationship



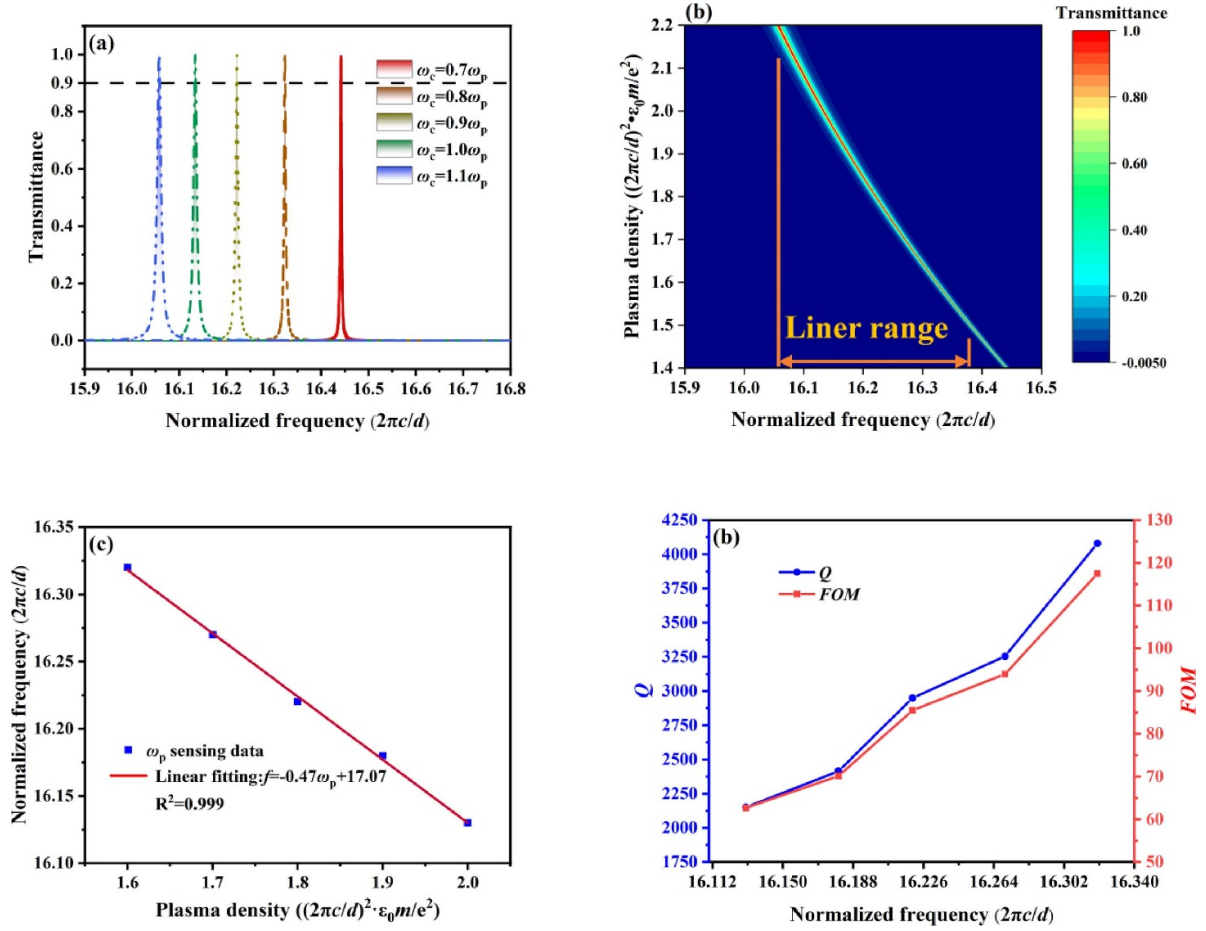


**Figure 5.** (a) The transmission spectra exhibit variations at different cyclotron frequencies of the electron. (b) The transmittance characteristics across the full frequency range are observed at varying thicknesses. (c) The transmission spectra are further analyzed after undergoing linear fitting. (d) The  $FOM$  and  $Q$  are assessed at different cyclotron frequencies of the electron.

with  $\omega_p$ . Figure 4(b) shows that within a continuous interval in the working frequency band 15–17 ( $2\pi c/d$ ), there is biased red filling, indicating that the high transmittance is greater than 0.9 at each  $\omega_p$  value, and most areas are dark blue, observing that at each working frequency point, there is only one transmission peak and no burrs. The efficiency of the sensor is greatly improved and ensures that it is not interfered with by other stray peaks during detection. The colored areas start thicker and become lighter, showing a strong linear relationship. Figure 4(c) further proves the linear relationship between frequency and the object being measured. The peak is extracted coordinates from figure 4(a) and performed linear fitting so that a strong linear relationship with a correlation coefficient greater than 0.996 is revealed. The specific linear fitting relation is  $S = 0.475 \text{ e} \cdot \text{m} \cdot \text{T}^{-1}$ , where e and m are on behalf of the number of charges and the relative mass of electrons

$$f_{\omega_p} = -0.475B + 17.99. \quad (57)$$

$Q$  and  $FOM$  are important physical quantities for measuring sensor performance, which can be easily calculated after obtaining  $S = 8.35 \times 10^{10} \text{ T}^{-1}$  from equation (57). In figure 4(d), the maximum values of  $Q$  and  $FOM$  are 4080 and  $117.5 \text{ e} \cdot \text{m} \cdot \text{T}^{-1}$ , and the minimum values are 2150.7 and

$62.7 \text{ e} \cdot \text{m} \cdot \text{T}^{-1}$ , both of which showed a rising trend within the working frequency range. In addition, the slope becomes larger during the rise of the value, indicating that the rate of change gradually increases with the change of frequency from 16 ~ 16.5 ( $2\pi c/d$ ). The overall performance of the sensor is good.

#### 4.2. About the plasma frequency

Based on the unique advantages of magnetized plasma materials, changes in  $PF$  can affect the overall RI, resulting in differences in phase and forming distinct transmission peaks across different working frequencies ranging from 15.9 to 16.5 ( $2\pi c/d$ ), with an initial parameter of  $\omega_p = 0.8\omega_0$ . By changing  $\omega_c$  from  $0.7\omega_p$  to  $1.1\omega_p$ , transmission spectra are plotted separately. As  $\omega_c$  decreased, the sharp transmission peak shifted gradually from left to right, and the density of the lines increased slowly, as depicted in figure 5(a). Figure 5(b) is a three-variable graph of frequency,  $PF$ , and transmittance, with colors changing from dark blue to bright red corresponding to transmittance values from 1 to 0. A quasi-linear curve is observed with an orange line in figure 5(c), with  $R^2 = 0.999$  and  $S = 0.47 (2\pi c/d)^{-1} \times e^2/m/\epsilon_0$ . After simplifying the

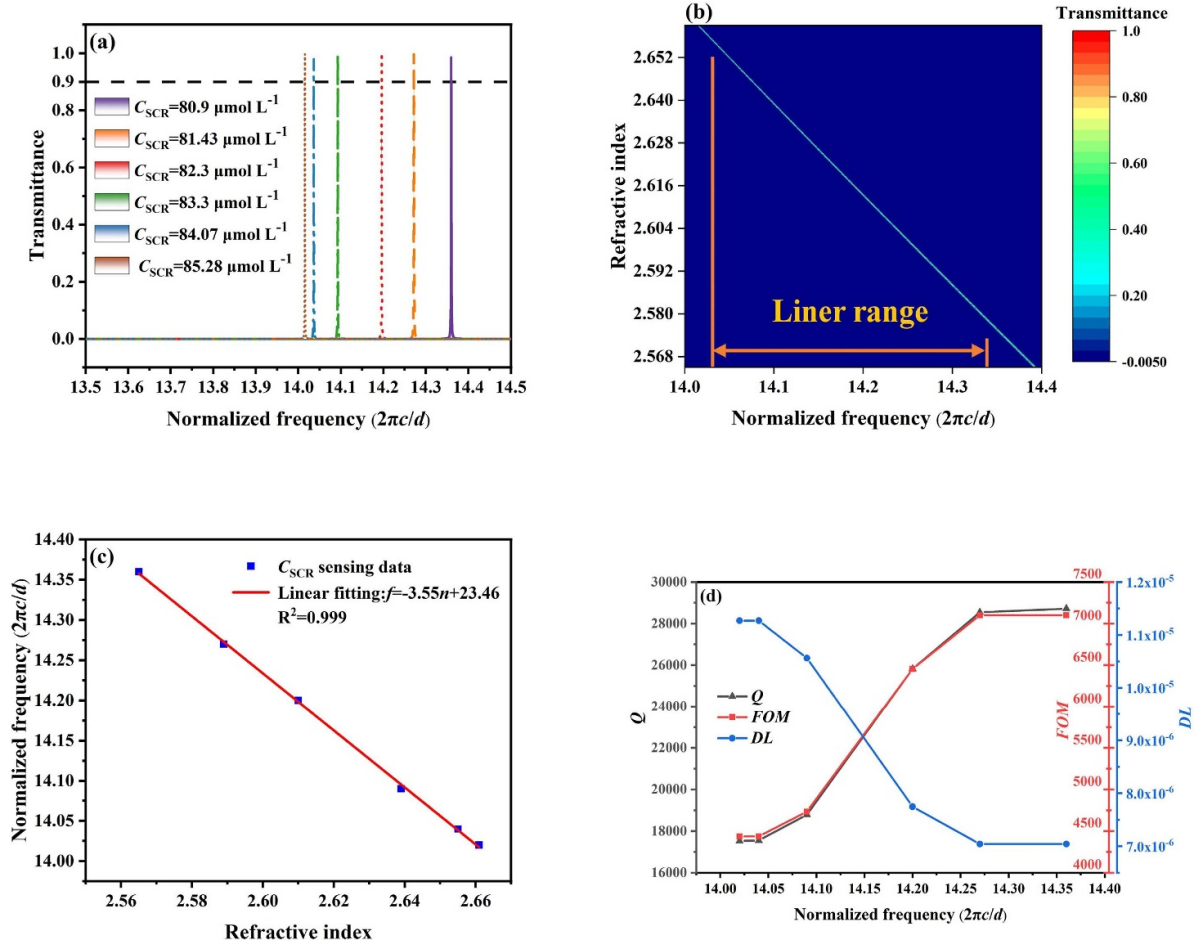


**Figure 6.** (a) The transmittance exhibits distinct peaks at different concentrations of the target analyte. (b) A three-dimensional overhead plan is presented, depicting the sensing capability of the sensor for different concentrations of the target analyte. (c) A linear relationship is established between the concentration of the target analyte and the corresponding resonance frequency. (d) The *FOM* and *Q* are evaluated at different concentrations of the target analyte.

calculation,  $S = 1.5 \times 10^{-4} (2\pi c/d)^{-1}$ . The specific linear formula is as follows:

$$f_{\omega_c} = -0.47\omega_p + 17.07. \quad (58)$$

Similar to the sensing performance of magnetic *B*, changes in *Q* and *FOM* values also demonstrated an upward trend, with a stable rising rate in figure 5(d). The maximum values of *Q* and *FOM* are as high as 6850 and  $198 (2\pi c/d)^{-1} \times e^2/m/\epsilon_0$ , respectively, with large standard deviations of 2101 and  $60.3 (2\pi c/d)^{-1} \times e^2/m/\epsilon_0$ . While not ideal, the mean values of 3583 and  $104.5 (2\pi c/d)^{-1} \times e^2/m/\epsilon_0$  remained consistent. As depicted in figure 5(a), the large standard deviation values of *Q* and *FOM* are due to the significant changes in half-high-frequency width across each curve. However, the overall sensor performance remained excellent and maintained a high level.

### 4.3. About the serum creatinine

Serum creatinine sensors hold immense significance in the field of healthcare due to their ability to provide precise and real-time measurements of serum creatinine levels [41]. These

sensors play a pivotal role in various critical aspects, including the assessment of kidney function, management of kidney diseases, personalized drug dosing, detection of acute kidney injury, post-transplant monitoring, and advancements in kidney research. By enabling accurate monitoring of serum creatinine levels, these sensors significantly enhance patient care, leading to improved treatment outcomes and a deeper understanding of kidney-related conditions. Their application facilitates the optimization of therapeutic interventions and contributes to advancements in renal medicine, benefiting individuals across diverse healthcare settings. When this structure is utilized for *C<sub>SC</sub>* detection, the initial parameters are set as  $\omega_p = 0.8\omega_0$  and  $\omega_c = \omega_p$ . The position of medium B is replaced with a serum creatinine solution and the solution concentration is subsequently changed to alter the *C<sub>SC</sub>* in the aqueous solution. As the *C<sub>SC</sub>* increases, the corresponding spectral lines shift in frequency from left to right. Additionally, each transmission peak value remains close to 1. These results are illustrated in figure 6(a). In essence, the sensing detection of *C<sub>SC</sub>* is the sensing of the equivalent RI of the solution, which is similar to the RI sensor. A close relationship between *C<sub>SC</sub>* and RI needs to be established, as shown in table 1 [42].

**Table 1.** Creatinine concentration ( $\mu\text{mol l}^{-1}$ ) with attributed RI.

RI	Creatinine concentration ( $\mu\text{mol l}^{-1}$ )
2.661	80.9
2.655	81.43
2.639	82.3
2.610	83.3
2.589	84.07
2.565	85.28

**Table 2.** The performance of published literatures compared with this work.

Literature	Multi-quantity measurement	Analyte	Performance			
			$S$	$Q$	$FOM$	$DL$
Su et al [44]	No	$B$	$6.5 \text{ nm T}^{-1}$	7602	5.5	$1.44 \times 10^{-5}$
Zaky et al [45]	Yes	Blood, cancer cells	72 THz/RIU	18.971	None	None
Bounaas and Labbani [46]	No	RI	11 THz/RIU	1420	407	None
Sriramprabha et al [47]	No	Chemical analytes	268 THz/RIU	None	1276	$3.9 \times 10^{-4}$
Wan et al [48]	No	RI	32.3 THz/RIU	None	100	None
Sun et al [49]	No	Plasmonic	0.95 THz/RIU	26.48	68	None
Zhang et al [50]	Yes	$B$	$1.45 \times 10^{10} \text{ T}^{-1}$	2235	None	None
		$PF$	$1 \times 10^2 (2\pi c/d)^{-1} \text{ m}^3$	1927	None	None
		RI	0.213 THz/RIU	378.03	None	None
This work	Yes	$B$	$8.35 \times 10^{10} \text{ T}^{-1}$	3583	105	None
		$PF$	$1.5 \times 10^{-4} (2\pi c/d)^{-1}$	2970	86	None
		$C_{SC}$	3.55 THz/RIU	22 824	5711	$9.19.1 \times 10^{-6}$

As a sensor design, when we detect a substance, we must have a very strong transmittance or absorptivity over a controlled frequency range, and this physical effect remains even when the measurement changes. The measurement of the structural efficiency of  $C_{SC}$  is specifically shown in figure 6(b). It can be observed that a thin and narrow linear function appears in the center of the image, which is distinguished by bright color and dark blue representing low transmittance. The thin and narrow properties can indirectly reflect the very cool sensing performance of this structure when it is used for  $C_{SC}$  material sensing, namely the  $Q$  value. To further explore the feasibility of the structure, five points are selected to be detected to study the relationship between peak frequency and material transformation in their transmission graphs, and found that there was a strong linear relationship with a correlation coefficient greater than 0.999. The specific linear fitting expression in figure 6(c) is shown below

$$f_{SCR} = -3.55C_{SC} + 23.46. \quad (59)$$

The  $S$  of the linear fitting formula is up to 3.55 THz/RIU, and the linear relationship is a negative correlation. Similar to the performance measurement standards of traditional sensors, they are often determined by the size of  $Q$  and  $FOM$ . The difference is that biosensor has a very high requirement on the  $DL$ , and the value should be less than  $10^{-4}$  [43]. The

sensor performance was calculated within the detection range, as shown in figure 6(d). The increasing and decreasing trends and rates of  $Q$  and  $FOM$  are relatively consistent, decreasing from 28 700, and 7100 RIU $^{-1}$  to 17 625, and 4438 RIU $^{-1}$ , respectively, and the variation range of performance within the detection range maintained at about 37% of the highest value. The variation curve of  $DL$ , contrary to  $Q$  and  $FOM$ , increases with the shift to the right of the corresponding peak frequency of the measured object, that is, the performance weakens, and the maximum  $DL$  reaches  $1.12 \times 10^{-5}$  RIU, still remaining below  $1 \times 10^{-4}$  RIU, which ensures the credibility of the structure for biosensing.

Last but not least, conventional sensors are often used only for single-physics measurements, dedicated to the fine measurement of a parameter. This paper proposes a multi-physics sensor, which can also be used for the measurement of different properties in the same structure. Additionally, the sensor in this paper has excellent  $Q$ ,  $FOM$ , and  $DL$  values, which are crucial for the fine measurement of multiple physical quantities. To highlight the features of the design of this paper, table 2 is used for comparison which focuses on the comparison of whether the multi-physical quantity sensor and the measurable physical quantity, and compares the corresponding sensor performance, highlighting the superiority of the MPSPC designed in this paper. While maintaining good  $S$ ,  $Q$ , and  $FOM$ , three kinds of physical quantities can be measured at the same time.

## 5. Conclusion

In summary, this paper proposes a multifunctional MPSPC sensor based on the evanescent wave principle and utilizes TMM for data simulation and calculation. The sensor can measure three physical quantities, including  $B$ ,  $PF$ , and  $C_{SC}$ , and the sensing performance for each physical quantity is discussed. The corresponding values of  $S$ ,  $Q$ , and  $FOM$  are  $8.35 \times 10^{10} \text{ T}^{-1}$ , 3583,  $105 \text{ e}\cdot\text{m}\cdot\text{T}^{-1}$  for  $B$ ,  $1.5 \times 10^{-4} (2\pi c/d)^{-1}$ , 2970,  $86 (2\pi c/d)^{-1} \times e^2/m/\epsilon_0$  for  $PF$ , and 3.55 THz/RIU, 22 824,  $5711 \text{ RIU}^{-1}$  for  $C_{SC}$ , respectively. As a  $C_{SC}$  biosensor,  $DL$  is the key detection index, reaching  $9.1 \times 10^{-6} \text{ RIU}$ . This paper broadens the use of PCs as a material and extends the design of photonic sensors, with a focus on deriving the formula of MPSPC. It is believed that the results presented in this paper will have practical applications in various fields in the future.

## Data availability statement

The data cannot be made publicly available upon publication because they are not available in a format that is sufficiently accessible or reusable by other researchers. The data that support the findings of this study are available upon reasonable request from the authors.

## Acknowledgments

This work was supported by the College Student Innovation Training Program of Nanjing University of Posts and Telecommunications.

## Conflict of interest

The authors declare no conflict of interest.

## ORCID iDs

Jie Xu  <https://orcid.org/0009-0003-4141-2570>

Hai-Feng Zhang  <https://orcid.org/0000-0002-9890-8345>

## References

- [1] Yablonovitch E 1987 Inhibited spontaneous emission in solid-state physics and electronics *Phys. Rev. Lett.* **58** 2059
- [2] John S 1987 Strong localization of photons in certain disordered dielectric superlattices *Phys. Rev. Lett.* **58** 2486
- [3] El-Naggar S A 2017 Photonic gaps in one dimensional cylindrical photonic crystal that incorporates single negative materials *Eur. Phys. J. D* **71** 1–6
- [4] Zhao Y, Shang L and Cheng Y 2014 Spherical colloidal photonic crystals *Acc. Chem. Res.* **47** 3632–42
- [5] Notomi M 2000 Theory of light propagation in strongly modulated photonic crystals: refractionlike behavior in the vicinity of the photonic band gap *Phys. Rev. B* **62** 10696
- [6] Kaliteevski M A, Brand S and Garvie-Cook J 2008 Terahertz filter based on refractive properties of metallic photonic crystal *Opt. Express* **16** 7330–5
- [7] Gilarlue M M, Badri S H and Saghai H R 2018 Photonic crystal waveguide intersection design based on Maxwell's fish-eye lens *Photon. Nanostruct. Fundam. Appl.* **31** 154–9
- [8] Gur D, Palmer B A and Weiner S 2017 Light manipulation by guanine crystals in organisms: biogenic scatterers, mirrors, multilayer reflectors and photonic crystals *Adv. Funct. Mater.* **27** 1603514
- [9] Yablonovitch E 1993 Photonic band-gap crystals *J. Phys.: Condens. Matter* **5** 2443
- [10] Mu C, Song J and Wang B 2018 Facile-synthesized carbonaceous photonic crystals/magnetic particle nanohybrids with heterostructure as an excellent microwave absorber *J. Alloys Compd.* **741** 814–20
- [11] Salehi M, Abbasian K and Pourziad A 2020 2D-photonic crystal based bowtie nano antenna designing with spherical gold particles for terahertz applications *2020 28th Iranian Conf. on Electrical Engineering (ICEE)* pp 1–4
- [12] Chen J, Xu L and Yang M 2019 Highly stretchable photonic crystal hydrogels for a sensitive mechanochromic sensor and direct ink writing *Chem. Mater.* **31** 8844–52
- [13] Mohammed N A, Khedr O E and El-Rabaie E S M 2023 Brain tumors biomedical sensor with high-quality factor and ultra-compact size based on nanocavity 2D photonic crystal *Alex. Eng. J.* **64** 527–40
- [14] Raghunathreddy M V, Indumathi G and Niranjana K R 2023 Silicon photonic microfluidic biosensor for monitoring renal dysfunction *J. Opt.* **34** 1–7
- [15] Miyan H, Agrahari R and Gowre S K 2022 Computational study of a compact and high sensitive photonic crystal for cancer cells detection *IEEE Sens. J.* **22** 3298–305
- [16] Cai Z, Kwak D H and Punihaole D 2015 A photonic crystal protein hydrogel sensor for *Candida albicans* *Angew. Chem.* **127** 13228–32
- [17] Jang K, Westbay J H and Asher S A 2022 DNA-crosslinked 2D photonic crystal hydrogels for detection of adenosine actuated by an adenosine-binding aptamer *ACS Sensors* **7** 1648–56
- [18] Watanabe K, Wu H Y and Xavier J 2022 Single virus detection on silicon photonic crystal random cavities *Small* **18** 2107597
- [19] Bertolotti M, Sibilica C and Guzman A M 2017 *Evanescent Waves in Optics: An Introduction to Plasmonics* vol 206 (Springer) pp 127–68
- [20] Luchansky M S and Bailey R C 2012 High-Q optical sensors for chemical and biological analysis *Anal. Chem.* **84** 793–821
- [21] Buisset C, Lépine T and Thiébaud E 2018 The evanescent wave coronagraph project: setup results and demonstrator preliminary design *Advances in Optical and Mechanical Technologies for Telescopes and Instrumentation III* vol 10706 pp 794–812
- [22] Basov S, Dankner Y and Weinstein M 2020 Noninvasive mid-IR fiber-optic evanescent wave spectroscopy (FEWS) for early detection of skin cancers *Med. Phys.* **47** 5523–30
- [23] Oheim M, Salomon A and Weissman A 2019 Calibrating evanescent-wave penetration depths for biological TIRF microscopy *Biophys. J.* **117** 795–809
- [24] Hu Y, Ghaffar A and Hou Y 2021 A micro structure POF relative humidity sensor modified with agarose based on surface plasmon resonance and evanescent wave loss *Photonic Sens.* **11** 392–401
- [25] Qi L 2012 Photonic band structures of two-dimensional magnetized plasma photonic crystals *J. Appl. Phys.* **111** 073301
- [26] Muggli P 2017 Beam-driven, plasma-based particle accelerators pp 119–42 ( arXiv:1705.10537v1)
- [27] Ham C, Kirk A and Pamela S 2020 Filamentary plasma eruptions and their control on the route to fusion energy *Nat. Rev. Phys.* **2** 159–67

- [28] Delanaye P, Cavalier E and Pottel H 2017 Serum creatinine: not so simple! *Nephron* **136** 302–8
- [29] Ni H, Zhou G and Chen X 2023 Non-reciprocal spatial and quasi-reciprocal angular Goos-Hänchen shifts around double CPA-LPs in PT-symmetric Thue-Morse photonic crystals *Opt. Express* **31** 1234–48
- [30] Baker J E, Sriram R and Miller B L 2015 Two-dimensional photonic crystals for sensitive microscale chemical and biochemical sensing *Lab Chip* **15** 971–90
- [31] El-Naggar S A 2020 Properties of defect modes in cylindrical photonic crystals *Optik* **200** 163447
- [32] Wang J and Zhu J 2013 Recent advances in spherical photonic crystals: generation and applications in optics *Eur. Polym. J.* **49** 3420–33
- [33] Kobayashi H and Okuno Y 2000 Feasibility study on frozen inert gas plasma MHD generator *IEEE Trans. Plasma Sci.* **28** 1296–302
- [34] Wang X, Fujimaki M and Awazu K 2005 Photonic crystal structures in titanium dioxide (TiO<sub>2</sub>) and their optimal design *Opt. Express* **13** 1486–97
- [35] Howell I R, Li C and Colella N S 2015 Strain-tunable one-dimensional photonic crystals based on zirconium dioxide/slide-ring elastomer nanocomposites for mechanochromic sensing *ACS Appl. Mater. Interfaces* **7** 3641–6
- [36] Hu C A, Wu C J and Yang T J 2013 Analysis of optical properties in cylindrical dielectric photonic crystal *Opt. Commun.* **291** 424–34
- [37] Huray P G 2011 *Maxwell's Equations* (Wiley)
- [38] Zhu T Q, Zhang J T and Zhang H F 2023 Investigation of photonic band gap properties of one-dimensional magnetized plasma spherical photonic crystals *Waves Random Complex Media* **48** 1–25
- [39] Wan B F, Zhou Z W, Xu Y and Zhang H F 2021 A theoretical proposal for a refractive index and angle sensor based on one-dimensional photonic crystals *IEEE Sens. J.* **21** 331–8
- [40] Wan B F, Wang Q Y, Peng H M, Ye H N and Zhang H F 2021 A late-model optical biochemical sensor based on OTS for methane gas and glucose solution concentration detection *IEEE Sens. J.* **21** 21465–72
- [41] Kumar D, Verma C, Dahiya S, Singh P K, Raboaca M S, Illés Z and Bakariya B 2021 Cardiac diagnostic feature and demographic identification (CDF-DI): an IoT enabled healthcare framework using machine learning *Sensors* **21** 6584
- [42] Aly A H, Mohamed D and Mohaseb M A 2020 Biophotonic sensor for the detection of creatinine concentration in blood serum based on 1D photonic crystal *RSC Adv.* **10** 31765–72
- [43] Sheehan E P and Lloyd J W 2005 Detection limits for nanoscale biosensors *Nano Lett.* **5** 803–7
- [44] Su D, Pu S and Mao L 2016 A photonic crystal magnetic field sensor using a shoulder-coupled resonant cavity infiltrated with magnetic fluid *Sensors* **16** 2157
- [45] Zaky Z A, Ahmed A M and Shalaby A S 2020 Refractive index gas sensor based on the Tamm state in a one-dimensional photonic crystal: theoretical optimization *Sci. Rep.* **10** 9736
- [46] Bounaas F and Labbani A 2020 High sensitivity temperature sensor based on photonic crystal resonant cavity *Prog. Electromagn. Res. Lett.* **90** 85–90
- [47] Sriramprabha R, Sekar M, Revathi R, Viswanathan C and Wilson J 2020 Fe<sub>2</sub>O<sub>3</sub>/polyaniline supramolecular nanocomposite: a receptor free sensor platform for the quantitative determination of serum creatinine *Anal. Chim. Acta* **1137** 103–14
- [48] Wan B F, Xu Y, Zhou Z W, Zhang D and Zhang H F 2021 Theoretical investigation of a sensor based on one-dimensional photonic crystals to measure four physical quantities *IEEE Sens. J.* **21** 2846–53
- [49] Sun B, Yu Y and Yang W 2020 Enhanced toroidal localized spoof surface plasmons in homolateral double-split ring resonators *Opt. Express* **28** 16605–15
- [50] Zhang J T, Rao S S and Zhang H F 2022 Multiphysics sensor based on the nonreciprocal evanescent wave in the magnetized plasma cylindrical photonic crystals *IEEE Sens. J.* **22** 10500–7